www.czasopisma.pan.pl PAN POLSKA AKADEMIA NAUK www.journals.pan.pl

Arch. Metall. Mater. **65** (2020), 1, 265-274

DOI: 10.24425/amm.2020.131726

E. POSTEK[1*], T. SADOWSKI[2]

HIGH-VELOCITY IMPACT OF 2-PHASE WC/Co COMPOSITE PLATE – BEGINNING OF THE PROCESS

2-phase composites are often used for high demanding parts that can undergo impact loads. However, most of the papers on dynamic loading concerns layered composites. In our opinion, the impact loads are not considered thoroughly enough. Good examples of 2-phase composites are: (1) a WC/Co cermet or (2) a monolithic ceramic Al_2O_3/ZrO_2. The WC/Co cermet is often modelled as having ductile elasto-plastic Co matrix and ideally elastic WC grains. It is because of very high crushing resistivity of the WC.

In this paper, we present an extension to earlier elaborated models ([44]) with the assumption of ideal elasticity of the grains. The new and general numerical model for high-velocity impact of the 2-phase composites is proposed. The idea of this novelty relies on the introduction of crushability of grains in the composite and thermo-mechanical coupling. The model allows for description of the dynamic response both composite polycrystals made of: (1) 2 different purely elastic phases (e.g. Al_2O_3/ZrO_2) or (2) one elastic phase and the second one plastic (e.g. cermet WC/Co), or (3) 2 elasto-plastic phases with different material properties and damage processes. In particular, the analysis was limited to the cases (2) and (3), i.e. we investigated the WC/Co polycrystal that impacted a rigid wall with the initial velocity equal to 50 m/s.

Keywords: 2-phase composites, cermet, Johnson-Cook plasticity, impact, numerical modelling

1. Introduction

Description of the microcracking process in the 2-phase composites is important for engineering applications and particularly for safety reasons during the exploitation of different structures, i.e. aerospace, mechanical and civil engineering. Majority of articles are concerned on a quasi-static micro-cracking response of different composites, e.g. in:

- different types monolithic polycrystalline ceramics (e.g. [1-9]) and ceramic matrix composites including small amount of porosity and other initial defects, e.g. [10-15],
- nanoceramic materials, e.g. [16,17],
- functionally graded materials, e.g. [18-25],
- cermets such as: tungsten carbide/cobalt (WC/Co) or titanium/molybdenum carbides, e.g. [26-33]
- polymer matrix composites, e.g. [34-37].

In this paper, the analysis was limited to the WC/Co polycrystal that impacted a rigid wall with a velocity equal to 50 m/s. Cermet, like WC/Co, is important for impact conditions because this composite is widely used for manufacturing of cutting tools applied in different branches of engineering. It was experimentally monitored for repeated dynamic compressive loading [38] and repeated impact load, [39]. Description of the dynamic loading of composites is presented for materials with a layered structure, [40]. High attention is paid to blast load or impact load, [41]. However, in our opinion, we have found a lack of references in modelling of the WC/Co composite during impact conditions. The dynamic analysis of the above cermet in the case of pulse pressure load and impact conditions is presented in [42,43].

This paper proposes an extension of earlier developed models of the WC/Co (e.g. [44]). In particular, our interest is focused on the models with elasto-plastic binders, elastic grains, elasto-plastic grains and assumption of micro-cracks initiation described by damage parameter D. The elasto-plastic material is modelled with Johnson-Cook plasticity, whereas the damage condition, associated with micro-cracks growth, is an extension of the plasticity model and is called the Johnson-Cook fracture model [45].

[1] INSTITUTE OF FUNDAMENTAL TECHNOLOGICAL RESEARCH PAN, 5B PAWIŃSKIEGO STR., 02-106 WARSZAWA, POLAND
[2] LUBLIN UNIVERSITY OF TECHNOLOGY, 40 NADBYSTRZYCKA STR., 20-618 LUBLIN, POLAND

* Corresponding author: epostek@ippt.pan.pl

2. Problem statement

2.1. Thermal equilibrium equation

An outline of the algorithm for solving a coupled thermo-mechanical problem using explicit time integration technique is given the Section. We give an outline of the algorithm, since not all details are described in the commercial software description. The thermal problem is described in the finite element form of a thermal equilibrium equation that fulfils boundary and initial conditions as follows,

$$\mathbf{KT} + \mathbf{C}\dot{\mathbf{T}} = \mathbf{F} \tag{1}$$

where **K** is the conductivity matrix, **C** is the heat capacity matrix, **T** is the nodal temperature vector, $\dot{\mathbf{T}}$ is the nodal temperature rate vector and **F** is the vector of thermal sources and fluxes. The thermal equation is solved explicitly, [46,53,54].

In our case, vector **F** includes only heat due to plastic dissipation. The finite element discretized mechanical problem is given in the form suitable for the explicit time integration, as follows,

$$\mathbf{M}\ddot{\mathbf{u}} + \mathbf{D}\dot{\mathbf{u}} = \mathbf{f} - \mathbf{p} \tag{2}$$

where **M** is the mass matrix, **D** is the damping matrix, **u** is the nodal displacement vector, $\dot{\mathbf{u}}$ is the nodal velocities vector, $\ddot{\mathbf{u}}$ is the nodal accelerations vector, **f** is the internal forces vector and **p** is the nodal loading vector. The central difference scheme for the Eq. (2) is given below, [53], with n denoting the current time step and Δt the time interval,

$$\ddot{\mathbf{u}}_n = (\operatorname{diag}\mathbf{M})^{-1}\left(\mathbf{f}_n - \mathbf{p}_n - \mathbf{D}\dot{\mathbf{u}}_n\right) \tag{3}$$

$$\dot{\mathbf{u}}_{n+1/2} = \dot{\mathbf{u}}_{n-1/2} + \ddot{\mathbf{u}}_n \Delta t \tag{4}$$

$$\mathbf{u}_{n+1} = \mathbf{u}_n + \dot{\mathbf{u}}_{n+1/2}\Delta t \tag{5}$$

From Eq. (1), the nodal temperatures vector reads,

$$\mathbf{T}_{n+1} = (\operatorname{diag}\mathbf{C})^{-1}\left(\mathbf{F}_n - \mathbf{K}_n\mathbf{T}_n\right) \tag{6}$$

Eq. (1) and Eq. (2) are solved simultaneously with central difference schemes given above, Eq. (3-6). The information between the systems is exchanged at each time step n. A new configuration is obtained with the assumption of fixed temperatures. The stability of the solution is checked at every selected time step.

The heat flux due to plastic dissipation is given by the formula,

$$f = \chi\, \boldsymbol{\sigma} : \mathbf{e}^{pl} \tag{7}$$

where f is the rate of heat generation, $\boldsymbol{\sigma}$ is the Cauchy stress tensor, $\mathbf{e}^{pl}$ is the rate of plastic deformation tensor and χ the Taylor-Quinney coefficient indicating fraction of plastic work converted into heat. We use the Johnson-Cook plasticity model that is described in the Section 2.2, therefore, the calculated Cauchy stress depends on temperature and plastic deformation, as well. It stands for the coupling term.

When concerning the elastic deformation due to temperature, the volumetric deformation is taken into account.

In the case of the adiabatic analysis, the thermal equation of equilibrium is neglected. The temperatures are obtained basing on Eq. (7), immediately.

2.2. The Johnson-Cook plasticity model

The Johnson-Cook plasticity model is given as follows,

$$\sigma^o = \left(A + B\left(\bar{\varepsilon}^{pl}\right)^n\right)\left(1 + C\ln\dot{\varepsilon}^*\right)\left(1 - \zeta^m\right) \tag{4}$$

where A is the yield stress, B is the hardening coefficient, C is the strain rate coefficient, n is the hardening exponent, m is the thermal softening exponent, $\dot{\varepsilon}^* = \dot{\varepsilon}/\dot{\varepsilon}_o$ is the dimensionless equivalent strain rate for $\dot{\varepsilon}_o = 1.0s^{-1}$. The dimensionless variable ζ that describes the temperature effect is given as follows,

$$\zeta = \begin{cases} 0 & \text{for} \quad T < T_{trans} \\ \left(T - T_{trans}\right)/\left(T_{melt} - T_{trans}\right) & \text{for} \quad T_{trans} \le T \le T_{melt} \\ 1 & \text{for} \quad T > T_{melt} \end{cases} \tag{5}$$

where T is the current temperature, T_{trans} is the temperature at which the yield stress dependence on temperature starts and T_{melt} is the melting temperature.

2.3. The Johnson-Cook fracture model

The Johnson-Cook fracture model is formulated as follows,

$$\varepsilon_p^f = \left(D_1 + D_2 \exp D_3\sigma^*\right)\left(1 + D_4 \ln\dot{\varepsilon}_p^*\right)\left(1 + D_5 T\right) \tag{6}$$

where ε_p^f is the equivalent plastic strains at fracture, $\dot{\varepsilon}_p^* = \sigma_m/\sigma$ is the non-dimensional pressure stress ratio with σ_m being pressure and σ meaning HMH stress. The parameters D_1, D_2, D_3, D_4 and D_5 are material constants that are evaluated experimentally.

The damage parameter D is defined as follows,

$$D = \sum \frac{\Delta\bar{\varepsilon}^{pl}}{\varepsilon_p^f} \tag{7}$$

where $\Delta\bar{\varepsilon}^{pl}$ is increment of equivalent plastic strain and ε_p^f is equivalent plastic strain at fracture that appears when $D = 1.0$.

3. Numerical model

The numerical model is developed from the model described in [45]. We use Abaqus program [46] for the calculations, MSC Patran for the model development [47] and GiD program for visualisation of the results [48].

The plate impacts a rigid wall with an initial velocity $v = 50$ m/s, Fig. 1 (a). The contact between the plate and the wall is frictionless. The discretisation of the plate is shown in Fig. 1(b). The polycrystalline composite structure is discretised with 41216

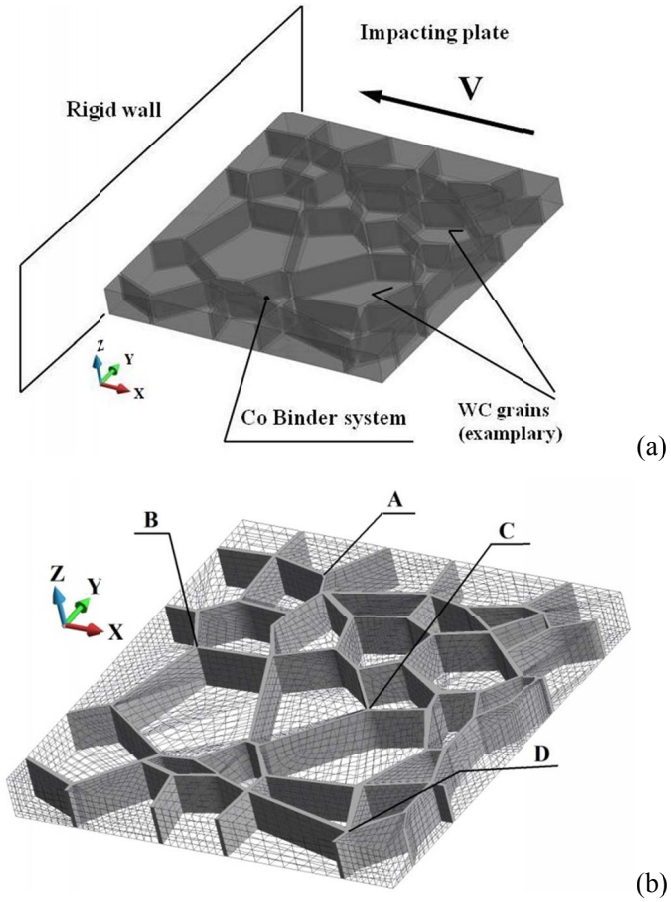

Fig. 1. (a) Impact scheme; (b) finite element mesh with binders system

nodes. The grains are discretized with 18882 elements and the binders are discretised with 15690 elements. We use the elements C3D8T for the fully coupled thermo-mechanical problem.

Material properties of the WC grains and Co binders are given in Tables 1 and 2, respectively.

In the paper, three variants of the polycrystalline material models were analysed, namely,

- Case A – elastic grains and elasto-plastic binders.
- Case B – elasto-plastic grains and elasto-plastic binders.
- Case C – elasto-plastic grains and elasto-plastic binders with in general 2 different damage mechanisms, i.e. both in grains and binders.

The material properties for (1) the cobalt in binders are taken from [49], whereas data for the WC grains are included in [50]. The basic properties of the WC/Co cermet components are presented in Tables 1 and 2. Besides, we assumed Taylor-Quinney coefficient as 0.9 for both materials. Due to the very low availability of the constants in the damage conditions, we assumed the same values of the constants for both phases of the cermet according to [50]. The constants in Eq. (5) are D_1, D_2, D_3, D_4, D_5 have the following values 0.0, 0.0019, –3.0, 0.0, 0.0, respectively.

The numerical results are obtained with the assumption of coupled thermo-mechanical solutions since the adiabatic solutions give too high temperatures due to not taking into account heat exchange between binders and grains [51]. The

TABLE 1

Parameters for the Johnson-Cook plasticity model for the WC grains

Parameter	Value
Young's modulus	6.2E+11 Pa
Poisson's coefficient	0.215
Yield stress (A)	3.0 GPa
Hardening coefficient (B)	89.0 GPa
Hardening exponent (N)	0.65
Strain rate coefficient C	0.0
Thermal softening exponent (M)	1.0
Melt temperature T_{melt}	1756 K
Transition temperature T_{trans}	293 K
Specific heat C_H	250 J/kg K
Thermal conductivity K	95 W/m K
Thermal expansion α_t	1.5E-05 1/K

TABLE 2

Parameters for the Johnson-Cook plasticity model for the Co binders

Parameter	Value
Young's modulus	2.1E+11 Pa
Poisson's coefficient	0.296
Yield stress (A)	3.97E+09 Pa
Hardening coefficient (B)	2.475 GPa
Hardening exponent (N)	0.31
Strain rate coefficient C	0.025
Thermal softening exponent (M)	1.0
Melt temperature T_{melt}	1356 K
Transition temperature T_{trans}	293 K
Specific heat C_H	240 J/kg K
Thermal conductivity K	150 W/m K
Thermal expansion α_t	5.0E-05 1/K

collection of maximum values of the considered field variables is given in Table 3.

TABLE 3

Maximum values of the field variables for Cases A, B, C polycrystalline models

Model	Displacement (m)	HMH stress (MPa)	Equivalent plastic strain (non-dim)	Temp (K)	D (non-dim)
A	3.31E-07	1942	0.610	315	x
B	8.61E-07	2853	1.186	336	x
C	62.2E-07	1693	0.00634	293	0.992

In the numerical results, we consider displacements fields, Huber-Mises-Hencky stress fields, equivalent plastic strain fields, damage parameter field, total reaction force, temperature fields and the energies. The energies are total energy ETOTAL, kinetic energy ALLKE, internal strain energy ALLIE, plastic strain energy ALLPD, damage energy ALLDM and internal heat energy ALLIHE.

4. Numerical results

4.1. Case A – purely elastic grains and elasto-plastic binders

Case A is the most conservative polycrystalline structure model. In this model, the WC grains are purely elastic. The assumption arises from the very high strength of the material. The cobalt binders are elasto-plastic.

When the WC/Co polycrystal impacts the rigid wall with the initial velocity of 50 m/s one can observe distinct discontinuities of the displacement field, Fig. 2(a). We note a recognisable line along the interfaces system inclined about 45° degrees that delimits the domains of lower and higher displacements. The line stands for the approximate sliding regions in the polycrystal (sliding lines).

The Huber – von Mises – Hencky reduced stress field is shown in Fig. 2(b). We note significant stress concentrations close to the junctions in the binder system. However, this reduced stress is not concentrated in the binders since the binders are elasto-plastic, but in the purely elastic grains. Plastic strains appear mostly in the binders, Fig. 3(a).

The temperature field is shown in Figure 3(a). The elevated temperature region covers most of the binder system since almost in all of the binders appear plastic strains. The increase in temperature also affects grains deformation due to heat conductivity, even though the followed time interval is quite short.

We observe equivalent plastic strain and temperature variation in the binder junctions A, B, C and D. We note that the highest equivalent plastic strain is in the junction A and the lowest in the junction D, Fig. 4(a). The same concens temperature, Fig. 4(b). We also note the temperature drop due to conduction effect. The highest temperature drop is in the junction A, and the lowest in the junction D. The junction A is the closest to the attacking edge of the sample while the junction D is the most far away from the attacking edge.

When concerning the total reaction force due to impact, Fig. 5, we note that it reaches the highest value at the beginning of the impact. The force decays; however, it reaches local maxima due to the presence of the large portion of the elastic material that constitutes the grains.

We present the dependences of total energy and internal heat energy. We note that internal heat energy grows and the internal heat energy becomes close to the total energy at the end of the observed time interval, Fig. 6(a). The kinetic energy decays at the time about 2.0E-08 s and slightly oscillates during the process, Fig. 6(b). The plastic strain energy grows during the process. The internal strain energy grows during the process with

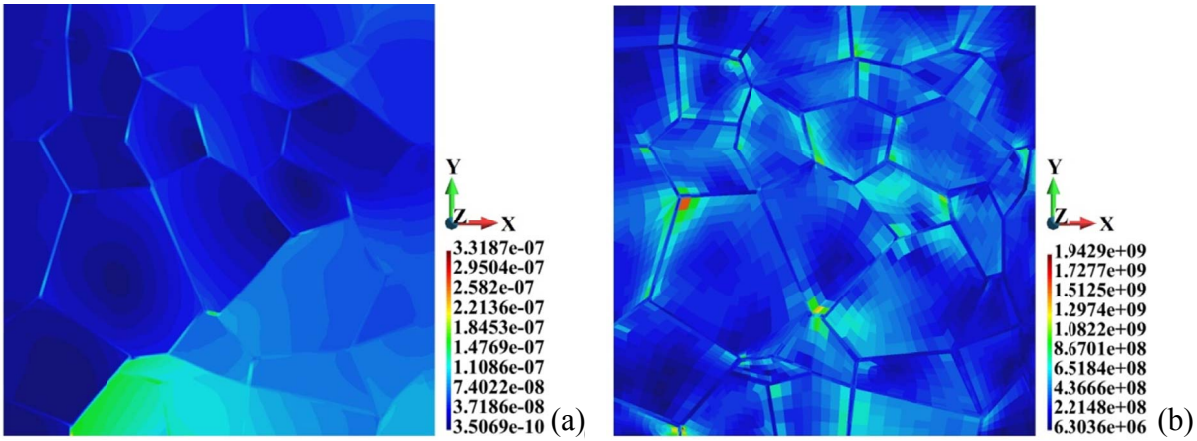

Fig. 2. Case A: (a) displacement field (m); (b) HMH stress field (Pa)

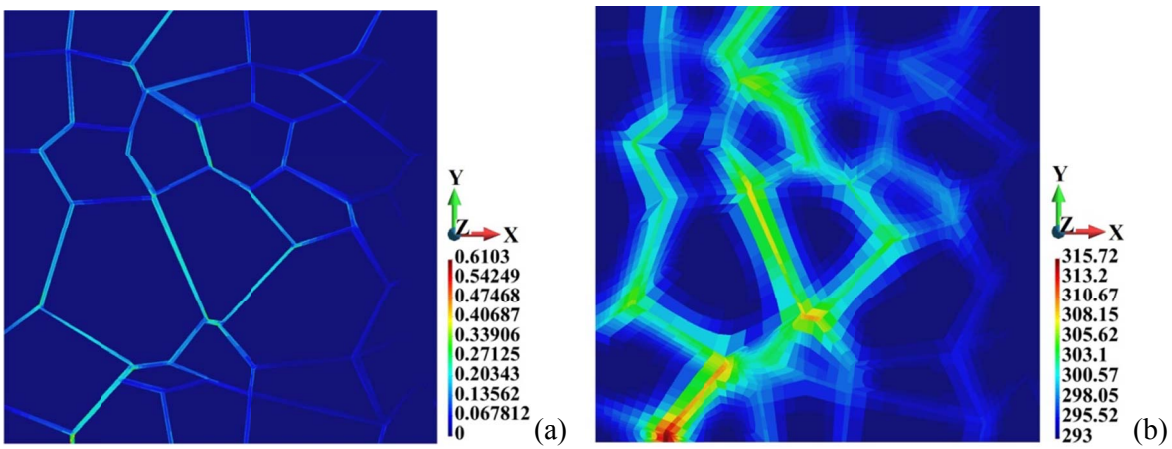

Fig. 3. Case A: (a) equivalent plastic strain field (non-dimensional); (b) temperature field (K)

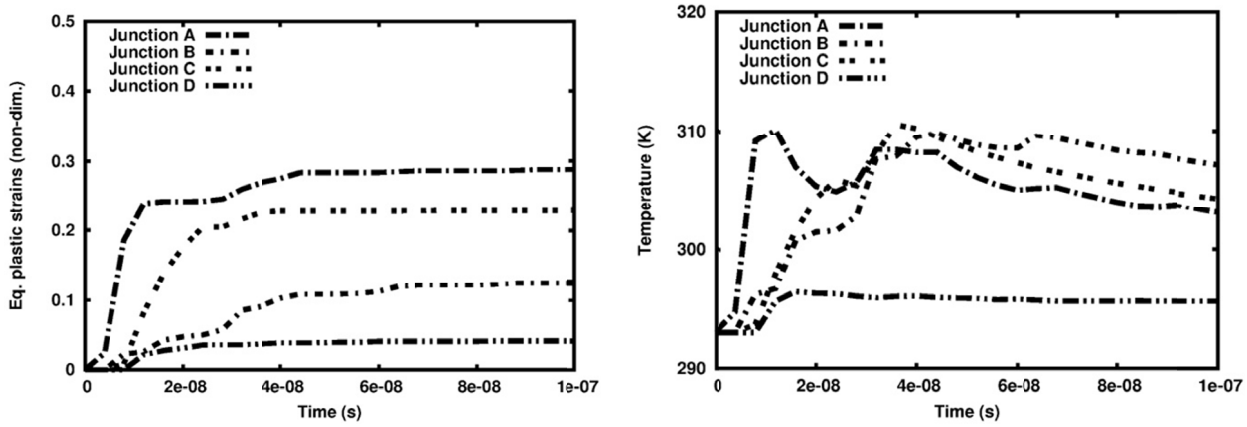

Fig. 4. Case A: Equivalent plastic strain time variation at the observed junctions (a) Temperature time variation at the observed junctions

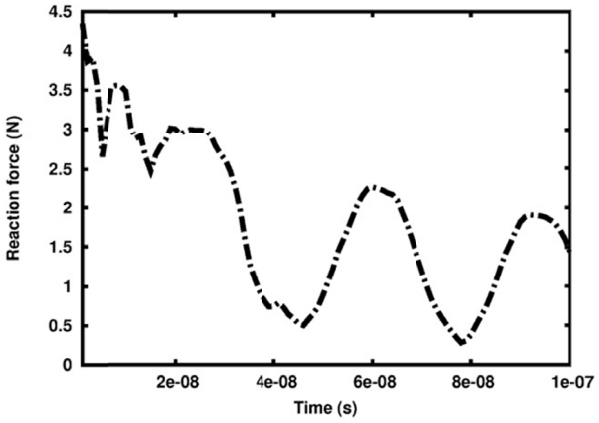

Fig. 5. Case A:Total reaction force (N) dependence on time

small oscillations. The value of the internal strain energy is of the range of the plastic strain energy, Fig. 6(b).

4.2. Case B – elasto-plastic grains and elasto-plastic binders

Further on, in Case B both phases of the polycrystalline material are elasto-plastic. In the experiments [50] it has been found that WC is basically an elasto-plastic material of a very high yield limit and a high hardening modulus.

When the WC/Co polycrystal impacts the rigid wall with the velocity of 50 m/s, it is possible to notice qualitative and quantitative differences in the variable fields.

We note that all of the maximum values in the observed fields are higher than in the Case A. Namely, displacements are 61% higher, the reduced stress – 23%, the equivalent plastic strains – 67%, temperature – 6%, Fig. 7(a), Fig. 7(b), Fig. 8(a), Fig. 8(b), respectively.

The displacement fields in Fig. 2(a) and Fig. 7(a) are different. In Case B, a distinct wedge is formed by the grains, that is in contrast to Case A.

In Case B, Fig. 7(b), the maximum Huber-von Mises-Hencky stress is higher than in Case A, Fig. 2(b). However, the reduced stress field is smoother than in Case A. The high values of the reduced stress are concentrated in the grains, but in contrast to Case A, they are not so strongly localised strictly nearby the binders junctions.

Equivalent plastic strain is significantly lower in the grains than in the binders, Fig. 9(a). The maximum equivalent plastic strain in grains reads 0.013, while in the binders we note 1.865. The same concerns the maximum temperature in the grains which is equal to 331°K, Fig. 6(b), while in the binders the relevant temperature values are slightly higher and equal to 336°K.

Equivalent plastic strain and temperature variation in time in the junctions A, B, C and D are given in Fig. 10(a) and Fig. 10(b), respectively. When comparing the dependences of the equivalent

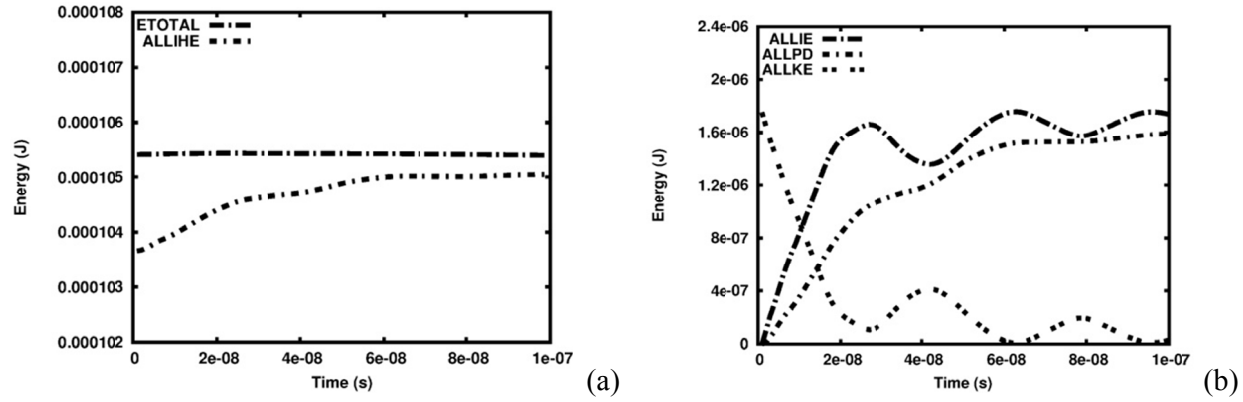

Fig. 6. Case A: Total energy and internal heat energy (a), internal strain energy, kinetic energy and plastic strain energy (b)

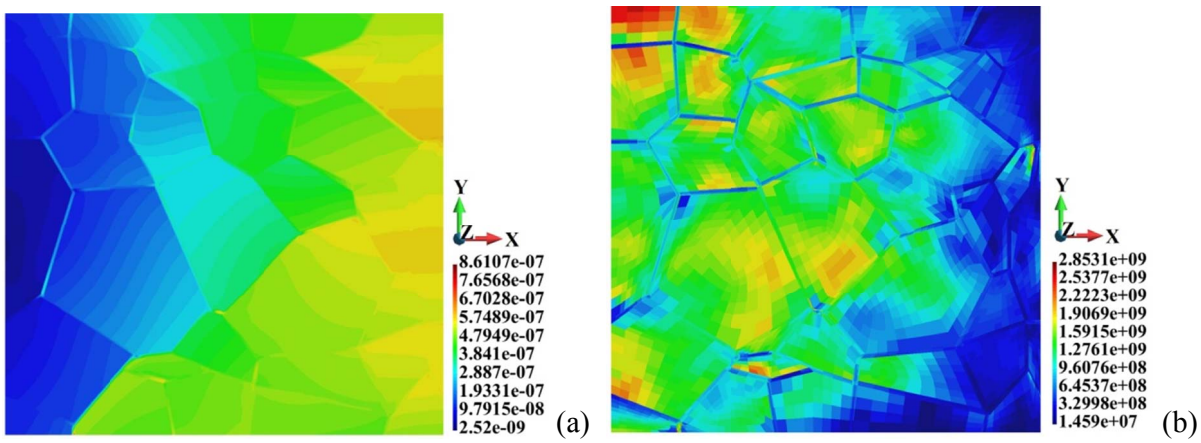

Fig. 7. Case B: (a) displacement field (m); (b) HMH stress field (Pa)

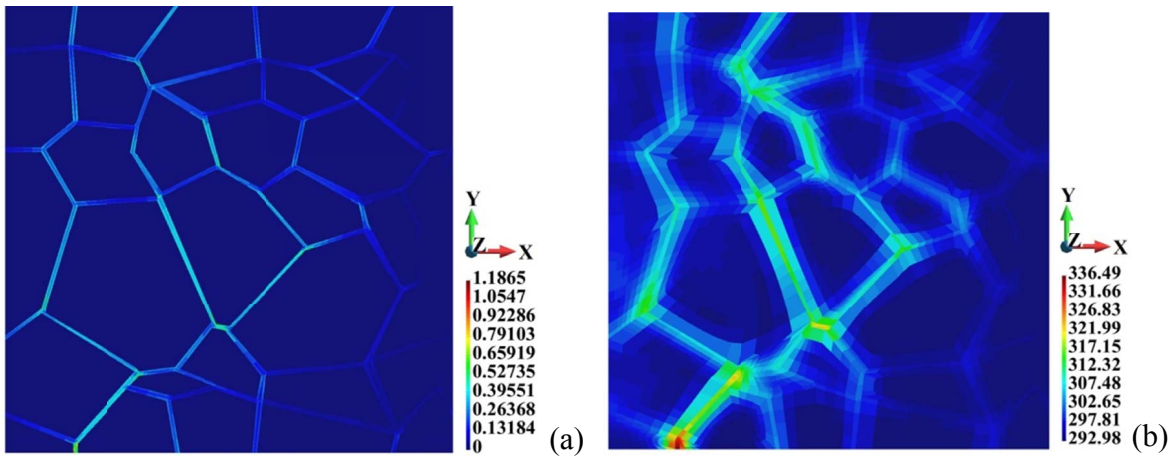

Fig. 8. Case B: (a) equivalent plastic strain field (non-dimensional); (b) temperature field (K)

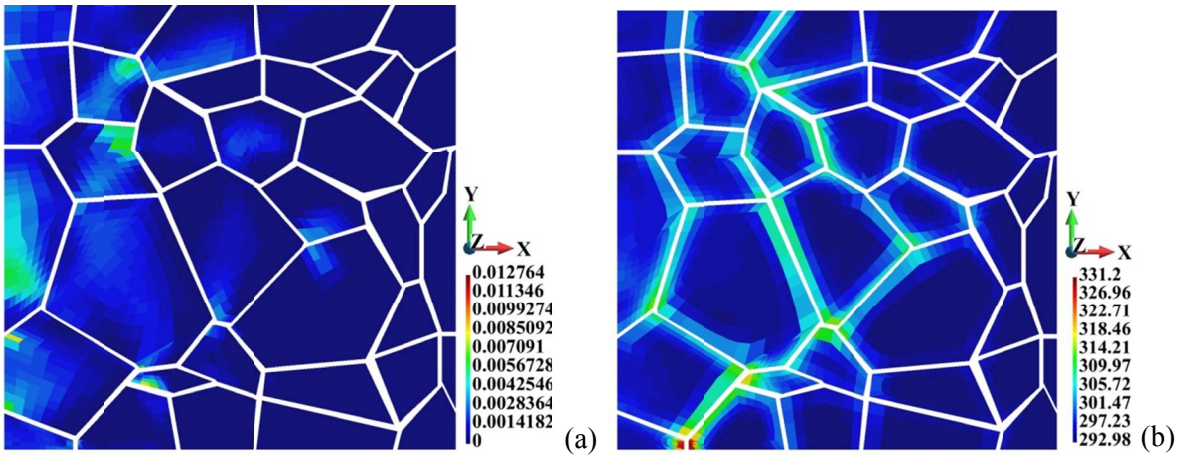

Fig. 9. Case B: (a) equivalent plastic strain field in the grains (non-dimensional); (b) temperature field in the grains (K)

plastic strain in the junctions with the Case A, we note that the maximum equivalent plastic strain is higher in the Case B in all of the junctions than in the Case A. However, the dependencies are qualitatively similar in both cases. In the observed junctions, the maximum temperature in the Case B is higher than in the Case A. The temperature drop is more significant in the Case B. In particular; it concerns the junction A. The values are higher because of the higher plastic strains in the Case B.

The total reaction force variations in Case A and B are qualitatively similar, Fig. 5 and Fig. 11. A small difference between the cases is that the first minimum of the force is at about 4.0E-08 s in the Case A while in the Case B the first minimum is later, namely at about 5.0E-08 s. The difference is due to lower stiffness of the plate because of arising plastic strains in both binders and grains.

Similarly to the Case A, the internal heat energy grows

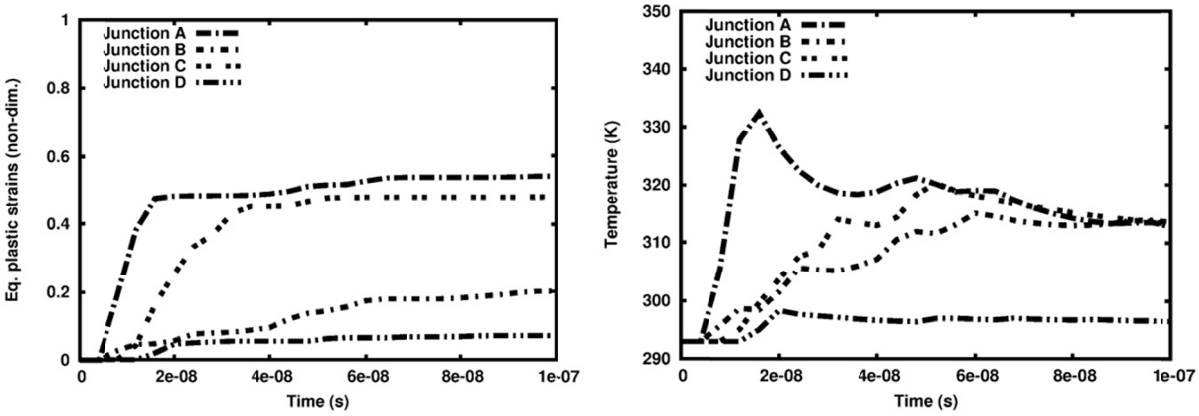

Fig. 10. Case B: Equivalent plastic strain time variation at the observed junctions (a) Temperature time variation at the observed junctions (K)

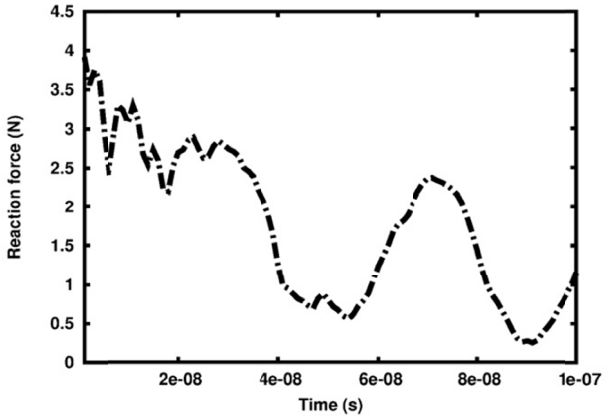

Fig. 11. Case B: Total reaction force (N) dependence on time

reaching the highest level at the end of the process. Participation of the internal heat energy grows and becomes the highest at the end of the time interval, Fig. 12(a). The variations of the internal strain energy, plastic strain energy and the kinetic energy are qualitatively similar to the Case A.

4.3. Case C – elasto-plastic grains and elasto-plastic binders with damage in grains and binders

When considering the possibility of damage in both phases of the polycrystalline structure, i.e. in the grains and the binders (Case C), the results become qualitatively different from Cases A and B.

The displacement field is given in Fig. 13(a). The maximum displacement is higher of 7.2 times than in Case B and 13 times higher than in Case A, respectively. We find sharp discontinuities in the displacement field approximately in the binders placed along the attacking edge. They are formed neither sliding line across the sample nor wedge.

The HMH stress is the highest in the grains abutting to the hitting bound of the sample, Fig. 13(b). The maximum Mises stress is lower than in the cases where the grains are perfectly elastic reading 35% of Case B and 12% of Case A. The equivalent plastic strains are much lower than in Cases A and B, Fig. 14(a). They appear in binders and grains. Since the plastic strains are very small, the increase in temperature is practically negligible reading 3°K, Fig. 14(b).

The key factor that changes the results qualitatively is damage parameter D. Microcracking process starts in these parts of polycrystal when the damage parameter D reaches values very close to 1.0. It is particularly visible in large part of the grains neighbouring the hitting edge, Fig. 15(a). The damage parameter is zero in the binders, Fig. 15(b).

Further analysis also shows that the behaviour of the structure is different from the Cases A and B. The reaction force is shown in Fig. 16(a). The reaction force oscillates about the level of 0.0012 N to the end of the process. However, the shortening of the time step shows that the reaction force reaches its maximum

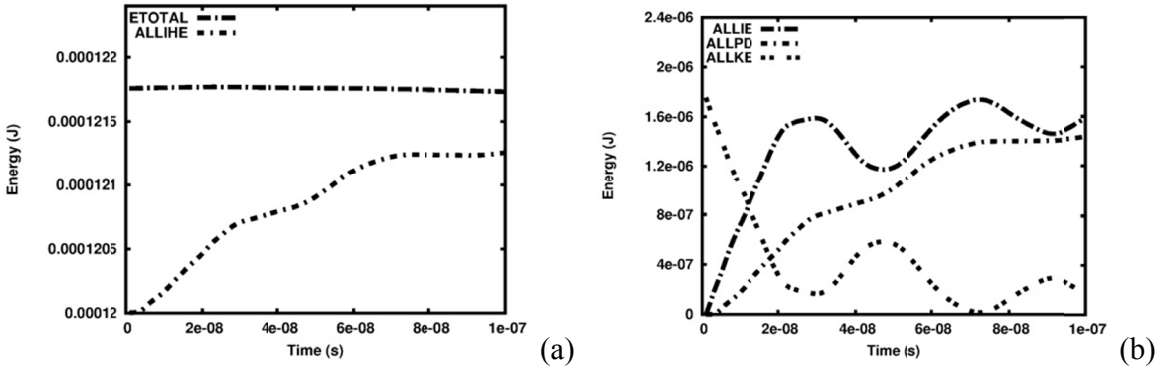

Fig. 12. Case B: Total energy and internal heat energy (a), internal strain energy, kinetic energy and plastic strain energy (b)

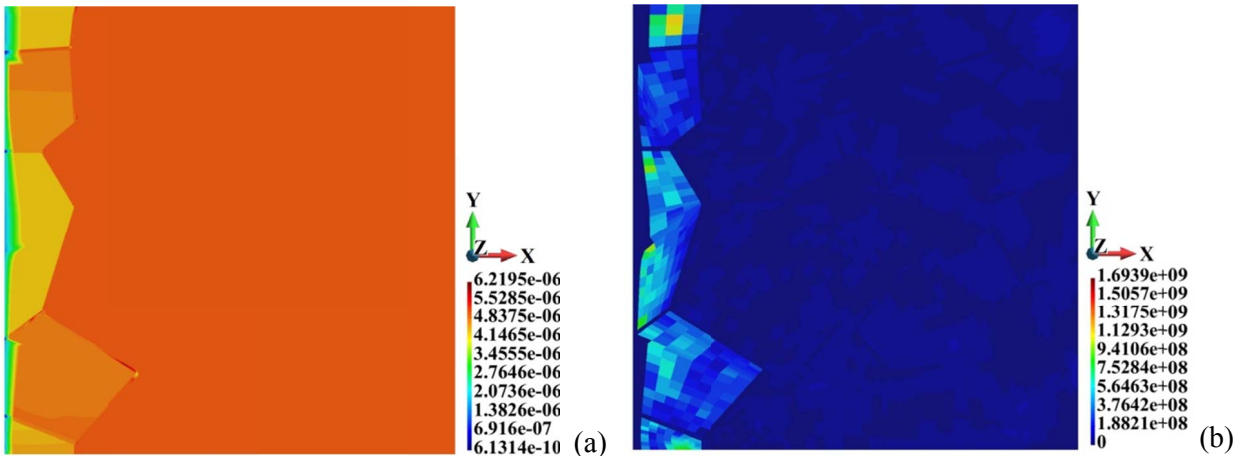

Fig. 13. Case C: (a) displacement field (m); (b) HMH stress field (Pa)

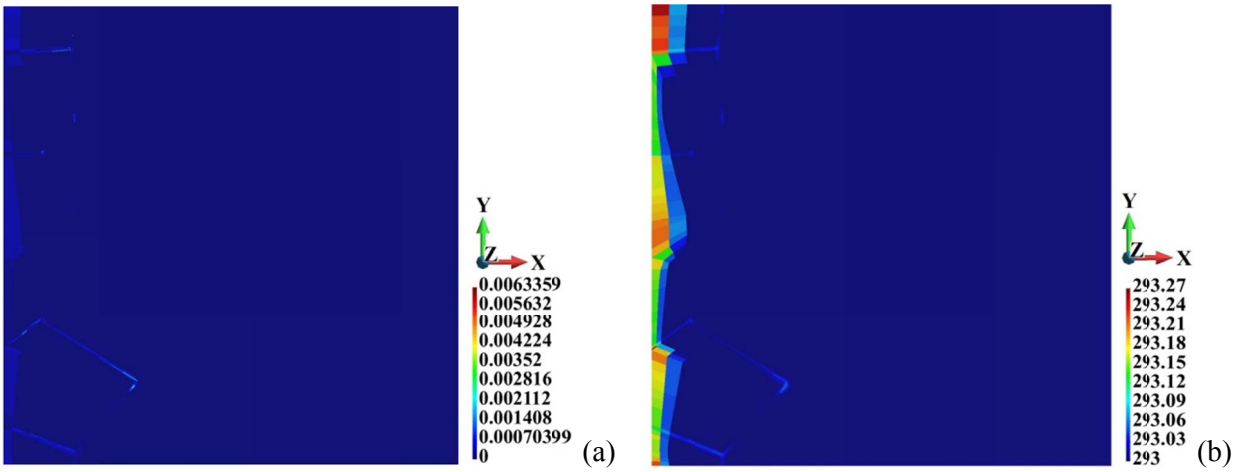

Fig. 14. Case C: (a) equivalent plastic strain field (non-dimensional); (b) temperature field (^{o}K)

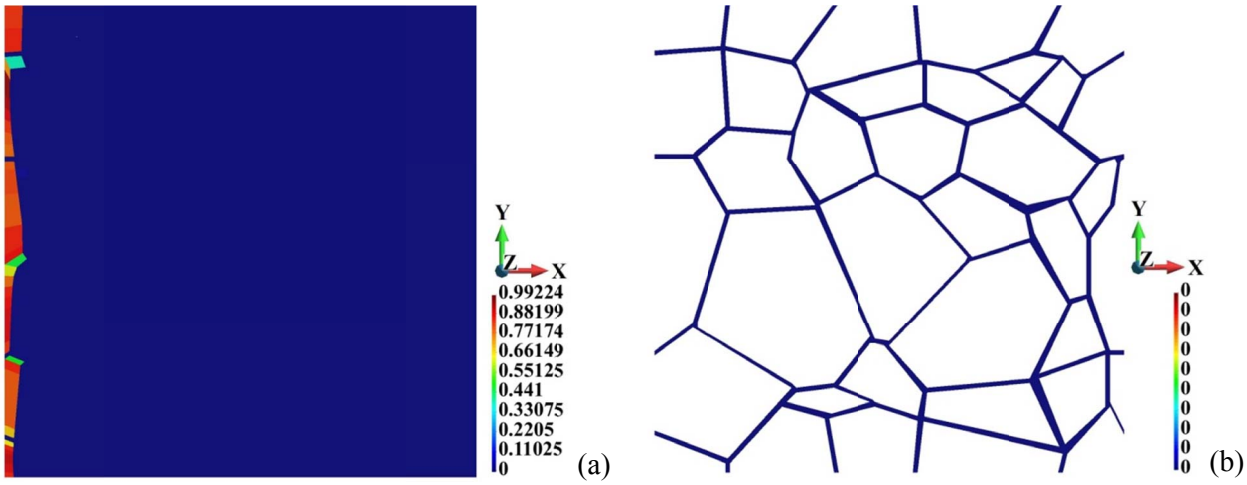

Fig. 15. Case C: damage parameter field (non-dimensional) in entire plate (a) and in the binders (b)

close to 2.88 N at 1.9E-10 s, Fig. 16(b). The reaction starts to decay immediately to the level 0.0012 N and oscillates.

The total energy and the internal heat energy are constant in the entire time interval, Fig. 17(a). They grow to their constant level in the 1.0E-09 s (not shown). The variation of the kinetic energy is shown in Fig. 17(b). It stabilizes at the time about 1.0E-09 s. The strain energy, plastic strains energy and damage energy reach their constant level at about 1.0E-09 s. We note that the process we can practically follow up to 1.0E-09 s. Further analysis will require the analysis of fragmentation that is beyond the scope of the considerations.

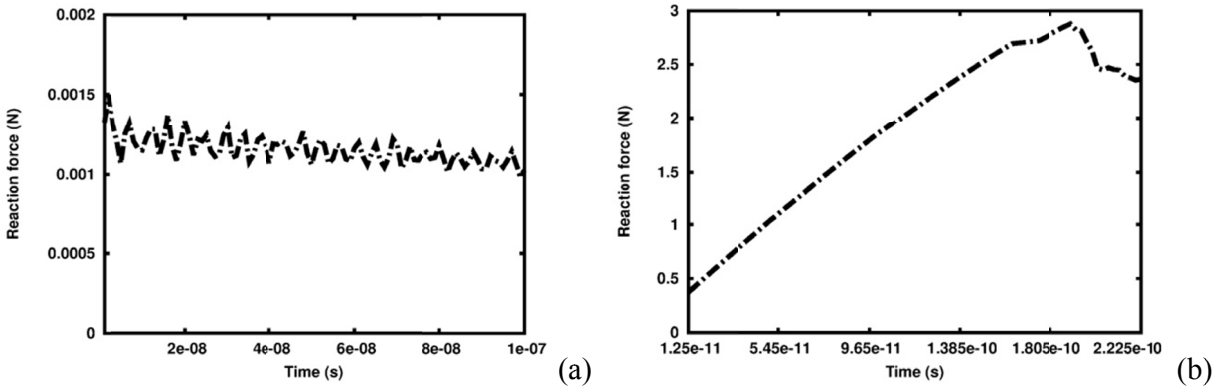

Fig. 16. Case C: Total reaction force dependence on time; entire time interval (a), enhanced time interval (b)

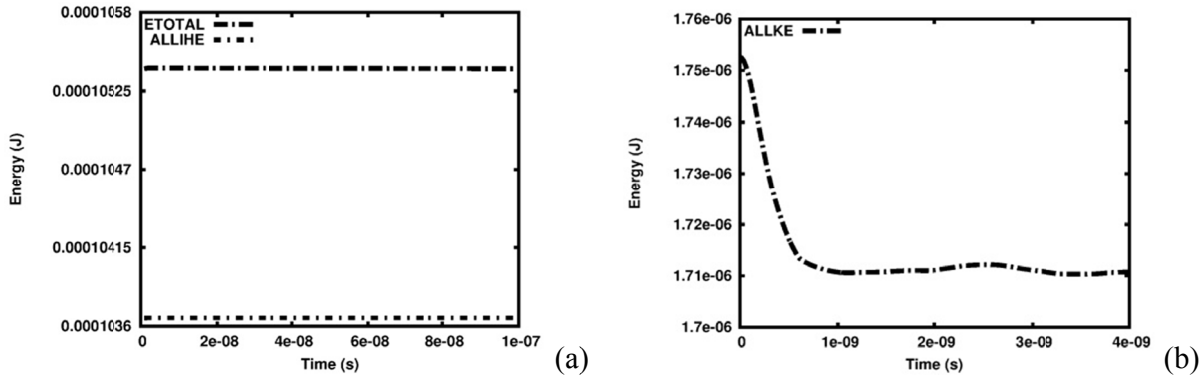

Fig. 17. Case C: Total energy and internal heat energy (a), kinetic energy (b)

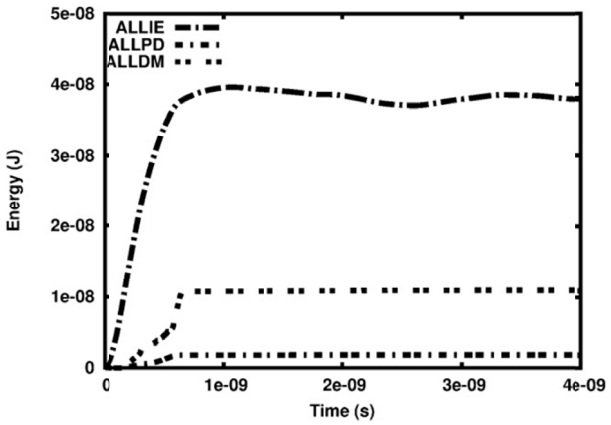

Fig. 18. Case C: Internal strains energy, plastic strains energy and damage energy

5. Summary

In the paper, the new numerical model for high-velocity impact of 2-phase polycrystals that impact the rigid wall with velocity of 50 m/s is proposed. The idea of this novelty relies on the introduction of crushability of grains in the composite and thermo-mechanical coupling. The model allows for description of the dynamic micro-cracking response of the composite polycrystals made of 2 phases: (1) different purely elastic phases (e.g. Al_2O_3/ZrO_2) or (2) one elastic phase and the second one plastic (e.g. cermet WC/Co), or (3) 2 elasto-plastic phases with different material properties and damage processes.

In particular, three variants of the WC/Co cermet modelling were analysed, showing the qualitative and quantitive difference between the three considered Cases of polycrystal behaviour under high velocity impact.

The important is the introduction of the damage condition into the Johnson-Cook plastic constitutive model, allowing for monitoring micro-cracks initiation and propagation in different parts of the polycrystalline structure.

The obtained numerical results lead to the formulation of the following conclusions for models without damage assumption (Cases A and B):

- impact response results in the high plastic strains and therefore high temperature,
- temperatures are elevated but not very high due to conductivity even at the beginning of impact process.

The conclusions corresponding to composite models with the inclusion of damage processes in both phases of the polycrystalline structures are the following:

- the equivalent plastic strains are significantly lower, therefore, the increase of temperature is low and practically negligible. It is valid for the beginning of the impact process,
- the displacements are the highest due to micro-cracking initiation and growth,
- all elevated values of the state variables are concentrated close to the hitting edge.

The model will be developed for more complicated internal composite structures. Currently, the dynamic damage response will be discussed for type material (1), i.e. for polycrystal made of 2 different purely elastic phases (e.g. Al_2O_3/ZrO_2), [52].

Acknowledgement

This work was financially supported by National Science Centre (Poland) project No 2016/21/B/ST8/01027 (Lublin University of Technology). Calculations are perfomed at the Interdisciplinary Centre for Mathematical and Computational Modelling in the University of Warsaw and at the Tricity Academic Supercomputer Centre in Gdańsk, Poland.

REFERENCES

[1] R.W. Rice. Porosity of ceramics. New York: Marcel Dekker Inc. 1998.
[2] T. Fett, D. Munz, Mechanical Properties, Failure Behaviour, Materials Selection, Ceramics. Berlin, Heidelberg, New York: Springer 1999.
[3] L.A. Gömze, L.N. Gömze, Ěpitöanyag – J. Silicate Based Comp. Mater. **61**, 38-42 (2009).
[4] T. Sadowski, S. Samborski, J. Am. Cer. Soc. **86**, 2218-2221 (2003).
[5] L.A. Gömze, L.N. Gömze, IOP Conf. Ser.: Mater. Sci. Eng. 47 012033
[6] T. Sadowski, Mech. Mater. **18**, 1-16 (1994).
[7] H.D. Espinoza, P.D. Zavatteri, Mech. Mater. **35**, 333-364 (2003).
[8] H.D. Espinoza, P.D. Zavatteri, Mech. Mater. **35**, 365-394 (2003).
[9] L. Marsavina, T. Sadowski, Int. J. Fract. **145**, 237-243 (2007).
[10] T. Sadowski, L. Marsavina, Comput. Mater. Sci. **6**, 209-211 (2009).
[11] T. Sadowski, Comput. Mater. Sci. **64**, 209-211 (2012).
[12] T. Sadowski, S. Samborski, Comput. Mater. Sci. **43**,75-81 (2008).
[13] D. Ghosh, M. Banda, S. Akurati, H. Kang, O. Fakharizadeh, Scripta Mater. **138**, 139-144 (2017).
[14] T. Sadowski, B. Pankowski, Comp. Struct. **143**, 388-394 (2016).
[15] T. Sadowski, J. Bęc, Comput. Mater. Sci. **50**, 1269-1275 (2011).
[16] M. Winter, Nanocrystalline ceramics, synthesis and structure. Berlin: Springer 2002.
[17] C.C. Koch, I.A. Ovid'ko, S. Seal, S. Veprek, Structural nanocrystalline materials: fundamentals and applications. Cambridge: Cambridge Univ. Press; 2007.
[18] S. Suresh, A. Mortensen, Fundamentals of functionally graded materials. Cambridge: The University Press; 1998.
[19] T. Sadowski, A. Neubrand, Int. J. Fracture **127**, 135-140 (2004).
[20] T. Sadowski, S. Ataya, K. Nakonieczny, Comput. Mat. Sci. **45**, 624-632 (2009).
[21] M. Birsan, T. Sadowski, L. Marsavina, D. Pietras, Int. J. Solids Struct. **50**, 519-530 (2013).
[22] T. Sadowski, P. Golewski, Comput. Mater. Sci. **52**, 293-297 (2012).
[23] T. Sadowski, P. Golewski, Comput. Mater. Sci. **64**, 285-288 (2012).
[24] V. Burlaynko, H. Altenbach, T. Sadowski, S.D. Dimitrova, Comput. Mat. Sci. **116**, 11-21 (2016).
[25] J. Gajewski, T. Sadowski, Comput. Mat. Sci. **82**, 114-117 (2014).
[26] L.S. Siegl, H.E. Exner, Metall. Trans. A **18A**, 1299-1308 (1987).
[27] L.S. Siegl, H.F. Fischmester, Acta Metall. **36**, 887-897 (1988).
[28] K.S. Ravichandran, Acta Metall. Mater. **42**, 143-150 (1994).
[29] S. Hönle, S. Schmauder, Comput. Mater. Sci. **13**, 56-60 (1998).
[30] F. Felten, G. Schneider, T. Sadowski, Int. J. Ref. Mat. Hard. Mat. **26**, 55-60 (2008).
[31] W. Li, H. Wang, L. Wang, C. Hou, X. Song, X. Liu, X. Han, Mater. Res. Letters **5**, 55-60 (2017).
[32] E. Postek, T. Sadowski, Comp. Interfaces **18**, 57-76 (2011).
[33] H. Dębski, T. Sadowski, Comput. Mater. Sci. **83**, 403-411 (2014).
[34] P. Robinson, E. Greenhalgh, S. Pinho, Failure Mechanisms in Polymer Matrix Composites, Woodhead Publishing; 2012.
[35] T. Sadowski, P. Golewski, M. Kneć, Comp. Struct. **122**, 66-77 (2014).
[36] T. Sadowski, E.M. Craciun, A. Rabaea, L. Marsavina, Meccanica **51**, 329-339 (2016)
[37] P. Wolszczak, T. Sadowski, S. Samborski, Comp. Part B **129**, 66-76 (2017)
[38] L. Krüger, K. Mandel, R. Krause, M. Radajewski, Int. J. Refract. Met. Hard. Mater. **51**, 324 (2015).
[39] Z.Q. Huang, L. Gang, Eng Fail Anal. **80**,273 (2017).
[40] L. Kärger, J. Baaran, A. Gunn, R. Thomson, Comp. Part B. **40**, 71 (2009).
[41] T.P. Vo, Z.W. Guan, W.J. Cantwell, G.K. Schleyer. Comp. Part B. **44**, 141 (2013).
[42] E. Postek, T. Sadowski, Comp. Struct. **203**, 498 (2018).
[43] E. Postek, T. Sadowski, Int. J. Refract. Met. Hard Mats. **77**, 68, (2018).
[44] T. Sadowski, S.J. Hardy, E. Postek, Mater. Sci. Eng. A. **424**, 230 (2006).
[45] G.R. Johnson, W.H. Cook, Eng. Fract. Mech. **21**, 31 (1985).
[46] Abaqus 6.13. User's Manual. http://dsk.ippt.pan.pl/docs/abaqus/v6.13/index.html
[47] MSC Patran http://www.mscsoftware.com/product/patran
[48] GiD http://www.gidhome.com/
[49] R.J. Hickman, J.L. Wise, J.A. Smith, J.P. Mersh, C.V. Robino, J.G. Arguello, in: AIP Conference Proceedings **1793**, 100018 (2017).
[50] T.J. Holmquist, G.R. Johnson, W.A. Gooch, WIT Transactions on Modelling and Simulation **40**, 61, 2005
[51] E. Postek, T. Sadowski, in: K. Wiśniewski, T. Burczyński (Eds), 41st Solid Mechanics Conference, Book of Abstracts, 106-107 (2018) Warszawa (PL).
[52] E. Postek, T. Sadowski, Impact models of two-phase composites, Advanced Materials Congress, 10-13 June 2019, Stockholm, Sweden – keynote lecture – accepted.
[53] J. Rojek, E. Onate, E. Postek, J. Mater. Process. Tech. **80-81**, 620, 1998.
[54] J. Rojek, O.C. Zienkiewicz, E. Onate, E. Postek, J. Mater. Process Tech. **119**, 41, 2007.